Title

Understanding 2p core-level excitons of late transition metals by analysis of mixed-valence copper in a metal—organic framework

Authors

Wang, Han

Su, Gregory M

Barnett, Brandon R

et al.

Publication Date

2024-04-04

DOI

10.1039/d4cp00662c

Peer reviewed

ARTICLE

Understanding 2p core-level excitons of late transition metals by analysis of mixed-valence copper in a metal–organic framework

Received 00th January 20xx,
Accepted 00th January 20xx

DOI: 10.1039/x0xx00000x

Han Wang[a,b,c,*], Gregory M. Su[c,d] Brandon R. Barnett[e,f,†], Walter S. Drisdell[c], Jeffrey R. Long[e,f,g] and David Prendergast[h]

The $L_{2,3}$-edge X-ray absorption spectra of late transition metals such as Cu, Ag, and Au exhibit absorption onsets lower in energy for higher oxidation states, which is at odds with the measured spectra of earlier transition metals. Time-dependent density functional theory calculations for Cu^{2+}/Cu^{+} reveal a larger 2p core-exciton binding energy for Cu^{2+}, overshadowing shifts in single-particle excitation energies with respect to Cu^{+}. We explore this phenomenon in a Cu^{+} metal-organic framework with ~12% Cu^{2+} defects and find that corrections with self-consistent excited-state total energy differences provide accurate XAS peak alignment.

Introduction

X-ray absorption spectroscopy (XAS) is a powerful tool for probing the chemical environment of a specific element within molecules and materials, directly accessing the electronic structure to reveal details of coordination number, angles between bonds, distances between neighboring atoms, and oxidation states[1–4]. In this work, we focus on the importance of XAS in revealing materials function – gas adsorption within metal-organic frameworks (MOFs) – and in distinguishing between oxidation states of a given element. XAS has often been applied to study changes in the population of mixed transition metal oxidation states, for example, in cathode materials for lithium-ion batteries[5–8], and has revealed a strong sensitivity to gas adsorption at active sites in MOFs[9].

The L_3 absorption edge ($2p_{3/2}$ excitations) of almost all transition metals in higher oxidation states appears at higher energies than that of the same metal in lower oxidation states. This is expected due to the increased binding energy of the corresponding 2p core orbitals in the more oxidized state, which is typically larger in magnitude than the difference in energy between the corresponding empty valence d orbitals accessed in the X-ray excitation. The same general trend is observed in K-edge spectra (1s excitations) and is the basis for an almost linear relationship between XPS peaks and oxidation state[10]. However, this trend is reversed in the late transition metals. Comparisons of the $L_{2,3}$-edge XAS of Cu_2O and CuO indicate a lower absorption edge for Cu^{2+} in CuO[11]. An analogous effect has been noted as unusual in the Ag L_3 edge of Ag_2O vs. AgO[12] and Fe L_2 edge of $K_4[Fe(CN)_6]$ vs $K_3[Fe(CN)_6]$[13]. *In situ* chemical variation has permitted similar differentiation between contributions of Au^{+} and Au^{3+} in solution-phase L_3-edge spectra[9]. Similar analysis may also assist in explaining the L_3-edge energy of the "mythical" d^8 state of Cu^{3+}, as recently discussed[14], which appears at higher energies than typical Cu^{2+} peaks, although we do not consider it here.

Variation in XAS signatures are extremely useful for revealing materials function. Recent work probing metal core-orbitals has revealed a strong sensitivity to gas adsorption at active sites in metal-organic frameworks (MOFs)[15]. MOF crystals are highly porous solids composed of metal ions connected by organic linkers with a broad suite of applications in gas storage[16–19], chemical separations[20–23], and catalysis[24–26]. In MOFs composed of transition metals, we may observe a range of oxidation states depending on the chemical environment around these atoms. Recently, in situ XAS uncovered the presence of oxidized Cu^{2+} defects in the MOF Cu^{I}-MFU-4*l* ($Cu_2Zn_3Cl_2$(btdd), H_2btdd = bis(1H-1,2,3-triazolo[4,5-*b*],[4',5'-*i*])dibenzo[1,4]dioxin), in addition to revealing the chemical bond between adsorbed gas molecules and open Cu^{+} sites, as defined by a strong XAS peak close to 935.3 eV. A pre-edge spectral signature, at a lower energy of 931.5 eV, was deduced to be Cu^{2+} based on measurements of the L_3-edge of known Cu^{2+} complexes and observations for standard Cu compounds (as stated above)[11]. Both oxidation states of Cu exhibit strong XAS transitions to orbitals with 3d character. Cu^{2+} has a nominal $3d^9$ valence

[a.] *School of Physical Science and Technology, ShanghaiTech University, Shanghai 201210, China *Email: wanghan3@shanghaitech.edu.cn*
[b.] *Center for Transformative Science, ShanghaiTech University, Shanghai 201210, China*
[c.] *Chemical Sciences Division, Lawrence Berkeley National Laboratory, Berkeley, CA 94720, USA*
[d.] *Advanced Light Source, Lawrence Berkeley National Laboratory, Berkeley, CA 94720, USA*
[e.] *Materials Sciences Division, Lawrence Berkeley National Laboratory, Berkeley, CA 94720, USA*
[f.] *Department of Chemistry, University of California, Berkeley, Berkeley, CA 94720, USA*
[g.] *Department of Chemical and Biomolecular Engineering, University of California, Berkeley, Berkeley, CA 94720, USA*
[h.] *The Molecular Foundry, Lawrence Berkeley National Laboratory, Berkeley, CA 94720, USA.*
† Current Affiliation: Department of Chemistry, University of Rochester, Rochester, New York 14627, USA
Electronic Supplementary Information (ESI) available.

electron configuration, with dipole-allowed 2p transitions possible into the empty 3d orbital. On the other hand, despite its nominal $3d^{10}$ electron configuration, the Cu^+ cation does exhibit noticeable 3d mixing with its ligands, resulting also in unoccupied orbitals with ligand-3d mixing and corresponding sharp XAS features at the Cu L_3 edge. Therefore, it is important to distinguish these contributions, which have different individual spectral intensities in order to draw quantitative conclusions from the XAS of mixed valence systems.

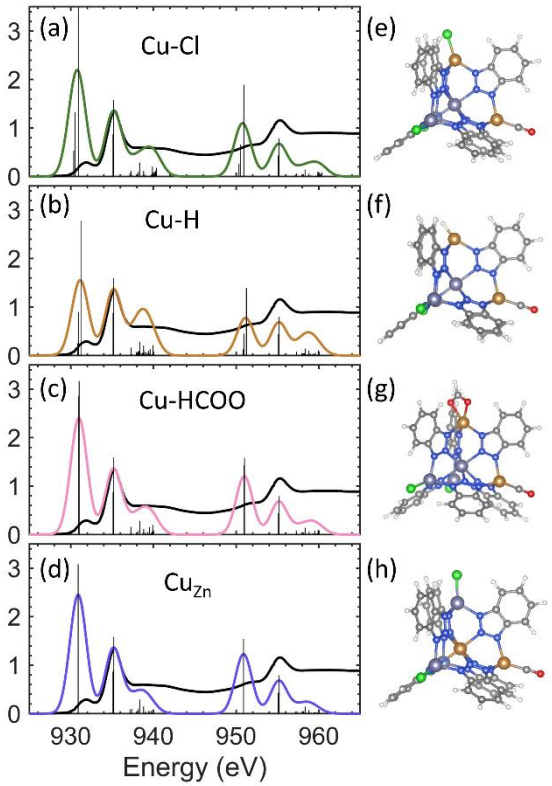

Figure 1. Calculated Cu L-edge XAS of CuI-MFU-4l with (a) Cl, (b) H, and (c) HCOO passivated Cu sites, and (d) Cu on Zn site substitution. The corresponding cluster geometries are shown in (e-h), respectively. Each cluster includes a Cu^{2+} and a Cu^+, and one CO molecule is absorbed on Cu^+. XAS for different adsorbates are shown in the SI. Black curves represent the experimental XAS of CO-bound CuI-MFU-4l, where the pre-edge peak (931.5 eV) originates from a much smaller population of Cu^{2+} overall, and the first main peak (935.3 eV) is due to Cu^+. The green, yellow, pink and blue curves represent the simulated spectra. The experimental results are from previous work ref[28]. The simulated spectra are all rescaled to fit the simulated first main peak intensity to experimental data.

Computational methods

Structural relaxation of the periodic MOF system was calculated using the Vienna Ab initio Simulation Package (VASP)[29,30], where the interactions between ion cores and valence electrons were described by the projector-augmented wave (PAW) method[31,32]. The vdW-DF2[33] functional was used for primitive cell optimization. A Hubbard U value of 10.4 eV for Cu 3d orbitals derived from the work of Gregory *et al.*[34] was used in addition to the vdW-DF2 functional. Γ-point sampling of the Brillouin zone and a plane wave kinetic energy cutoff of 400 eV are used for all variable-cell calculations. The experimental lattice constant of the bare framework is 31.21 Å at room temperature. To reduce computational cost, we considered a unit cell with a higher order of symmetry, and we could obtain a smaller primitive cell with a lattice constant of 22.069 Å and lattice angle of 60°, as shown in Fig S1(a).

To enable localized atomic orbital calculations of the XAS, we derived finite cluster models from the periodic structure. Clusters with only two Cu atoms at each ligand-MOF junction were generated from the periodic framework structure by replacing the $btdd^{2-}$ ligands with terminal benzotriazolate groups. The local coordination environment around Cu before attaching any molecules is of C_{3v} symmetry. The def2-SVPD[35] basis-set was used for Cu and N atoms in the MOF cluster and for atoms on the guest molecules , while the def2-SVP basis set was used for the remaining atoms.

X-ray absorption spectra were calculated using the reduced single excitation space[36] linear-response time-dependent density-functional theory (LR-TDDFT)[37] method implemented within Q-Chem[38]. The ωB97M-V functional was used to relax the cluster structure and to perform the XAS LR-TDDFT calculations. These LR-TDDFT calculations do not include spin–orbit coupling effects. To construct the combined $L_{2,3}$-edge spectrum, the calculated L_3-edge spectrum is augmented by addition of a copy of the same spectrum which is displaced on the energy axis by +20.0 eV (the atomic spin-orbit splitting for Cu 2p) and rescaled in intensity to 50%, to reflect the L_2- and L_3-edge splitting and the simplest branching ratio of spin-orbit split Cu 2p orbitals (i.e., 2:4), respectively. This approach is appropriate here based on the relatively large core-orbital spin-orbit splitting of Cu and insignificant valence-orbital spin-orbit corrections.

Results and discussion

Four potential chemical environments for Cu^{2+} at the peripheral framework metal sites were investigated: Cu–Cl; Cu–HCOO; Cu–H and Cu_{Zn} [Fig. S1(b)-(e)]. The first two possibilities were considered the most likely environments for Cu^{2+} given that the synthetic route used to produce Cu^{I}-MFU-4*l* exploits post-synthetic exchanges with $CuCl_2$ and LiOC(O)H[39,40]. For completeness, we included hydride-terminated Cu^{2+} given the predisposition of metal-bound formates to undergo thermal decarboxylation[39,41,42] and the substitution of Zn^{2+} for Cu^{2+} at the octahedrally-coordinated site at the center of the node, although this environment was deemed unlikely owing to the reluctance of coordinatively-saturated metals to undergo cation exchange[43].

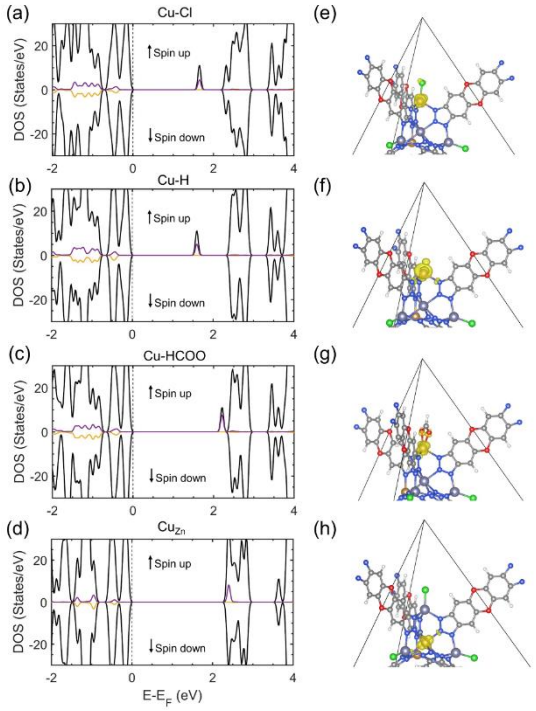

Figure 2. The PDOS of Cu^{I}-MFU-4*l* with (a) Cl, (b) H, and (c) HCOO passivated Cu sites, and (d) Cu on Zn substitution. The purple and yellow lines represent the projection to Cu 3d spin-up and spin-down orbitals, respectively. The corresponding charge density of the in-gap states are shown in (e-h), respectively. Valence band maximum (VBM) energy is set to 0 eV.

The comparison between the simulated and experimental XAS and related cluster geometries are shown in Fig. 1. We employed density functional theory (DFT) for ground state electronic structure and geometry relaxation and linear-response time-dependent DFT (LR-TDDFT) for X-ray spectral simulations. Each cluster used for the simulations has one CO molecule attached at the Cu^+ sites. The black curves report the experimental XAS of Cu^{I}-MFU-4*l* in a 0.25 mbar atmosphere of CO. The adsorption of CO is expected to reach saturation in this MOF and cover all Cu^+ sites[28]. We noticed only small differences in atomic geometry with respect to varying the exchange-correlation (XC) energy functional used in the geometry relaxation, and, in general, the electronic structure follows our intuition for the distinct oxidation states of the Cu sites.

All previous measurements exhibit a small pre-edge feature at 931.5 eV[28], which is due to the presence of Cu^{2+}. The first main peak emerges at about 935.3 eV, and is attributed to the antibonding orbital between the CO lowest unoccupied molecular orbital (LUMO) and a Cu 3d orbital. In addition, as shown in Fig. S2 and S3, Cu^{2+} don't contribute to the first peak and the Cu-CO antibonding orbital doesn't contribute the pre-edge peak, which is consistent with previous experimental result[11]. The Cu^{2+} to Cu^+ concentration ratio in the simulated clusters is 1, by construction. This allows us to see the relative intensity of their spectral contributions before we factor in their relative population. We use this information later to estimate the true concentration ratio, which is about one order of magnitude lower in experiment, according to the analysis later in this work.

Table 1. The dependence of various components of the XAS excitation energy on various hybrid functionals: pre-edge peak to first main peak energy difference, pre-edge peak binding energy ($E_{\text{binding}}^{\text{pre-edge}}$), first main peak binding energy ($E_{\text{binding}}^{main}$), 2p orbital energy ($\varepsilon_{2p}$) difference, Cu^{2+} Mulliken charge, Cu^+ Mulliken charge, HOMO-LUMO gap, in-gap-state-HOMO gap. The M06-2X, PBE0, ωB97M-V, HSE functionals and customized functionals with 15%, 20% and 54% HF exchange contributions are utilized. The cluster calculated is a cluster with one Cu^+ attached with CO and one Cu-Cl.

Published XC Functional / customized functional exact exchange ratio	ωB97 M-V (short range 15 %, long range 100% HF)	HSE (short range 25%, long range 0 % HF)	M06 -2X (54 % HF)	15%	20%	PBE0 (25 % HF)	54%
Pre-edge peak to first peak energy difference (eV)	4.27	4.63	9.48	3.43	4.01	4.65	9.31
Pre-edge peak exciton binding energy (eV) ($E_{\text{binding}}^{\text{pre-edge}}$)	11.38	6.87	17.99	3.65	5.26	6.96	18.16
First main peak exciton binding energy (eV) ($E_{\text{binding}}^{main}$)	5.50	1.34	5.04	1.09	1.60	2.09	4.93
2p orbital energy (ε_{2p}) difference, Cu^{2+} vs. Cu^+ (eV)	2.85	2.36	4.48	1.60	1.98	2.39	4.43
Cu^{2+} charge	0.59	0.63	0.76	0.55	0.59	0.63	0.85
Cu^+ charge	0.12	0.11	0.36	0.05	0.08	0.11	0.29
HOMO-LUMO gap (eV)	9.06	4.29	6.91	4.38	4.70	5.08	7.10
in-gap-state-HOMO gap (eV)	7.07	2.09	6.12	1.85	2.34	2.85	6.77

From our simulations, we observe that for the Cu-H case, the pre-edge peak to first main peak intensity ratio is close to one, whereas for the other cases considered (Cu-Cl, Cu-HCOO, and Cu_{Zn}), the pre-edge peak is more intense than the first main peak. We will show below that the stronger intensity of the pre-edge peak is due to the more ionic bonds in these latter cases, which preserve the $3d^9$ configuration of the Cu^{2+} cation. In other words, there is a hole on the Cu site from the Cu 3d orbital subspace which is accessible by dipole-allowed transitions from Cu 2p core orbitals. By contrast, the coupling between Cu^+ and adsorbed molecules (such as CO, NH_3, etc.) involves some degree of covalency or orbital mixing and the coupling strength is relatively weak. For this reason, the spectrally accessible antibonding orbitals only show a small fraction of Cu 3d

character. Even if Cu had different coordinations, the Cu^{I} related XAS peaks signal should depend strongly on the presence of attached molecule as long as Cu has a nominal $3d^{10}$ configuration. Using relative XAS intensity as a measure of the strength of bonding, this implies that the Cu-H bond is weaker (or at least involves less orbital mixing) than the more ionic Cu-Cl and Cu-HCOO bonds.

The projected density of states (PDOS) of the MOF with Cu-Cl, Cu-H, Cu-HCOO, and Cu_{Zn} defects are shown in Fig. 2. In the Cu-Cl, Cu-H, Cu-HCOO case, the attached group occupies the space near Cu^{2+} and the Cu atom will not be able to adsorb any CO molecule. In addition, our later analysis shows that CO is not involved with the pre-edge peak, so we don't include any CO molecule in the PDOS calculation. The occupied Cu 3d orbitals are located near the valence band maximum (VBM) in the pristine MOF and the VBM is dominated by oxygen 2p orbital character from the ligands. However, when oxidizing groups bind to the Cu site (Cl, H, HCOO), an empty Cu 3d orbital appears within the band gap, indicating that the oxidation state of Cu is now formally 2+. Since these unoccupied in-gap states have localized Cu 3d character, they will already define strong optical transitions in the $L_{2,3}$-edge XAS experiment before absorbing any CO molecules. By contrast, in the Cu^{+} case, occupied Cu 3d orbitals form a weak bond with the adsorbate (CO) through mixing with its orbitals. The corresponding unoccupied antibonding orbital energy is higher than both the Cu 3d orbital and the CO LUMO level, placing it above the conduction band minimum (CBM) of the MOF, as shown in Fig. 3.

We found significant variations in the XAS simulations resulting from LR-TDDFT employing various density functional approximations, including M06-2X, ωB97M-V, PBE0, HSE, and customized functionals with global HF exchange, α, of 15, 20, or 54%. We can use details of these variations to pick an optimal functional for XAS and to understand the origins of the energy ordering of the L_3 edges. We divide the various contributions to the energy of a specific 2p core-excited state f of atom I as follows:

$$E_{XAS\ peak} \sim \varepsilon_f - \varepsilon_{2p} - E_{\text{binding}}, \qquad (1)$$

where ε_{2p} is the Kohn–Sham orbital energy of the 2p core electrons, ε_f is the dominant valence Kohn–Sham virtual orbital energy of the corresponding LR-TDDFT root, with their difference defining a non-interacting excitation energy, while E_{binding} is the attractive core-exciton binding energy, which lowers the energy of the observed XAS peak. Differences in the core-excitation energies of atoms in different oxidation states will be discussed in terms of differences between each of these terms:

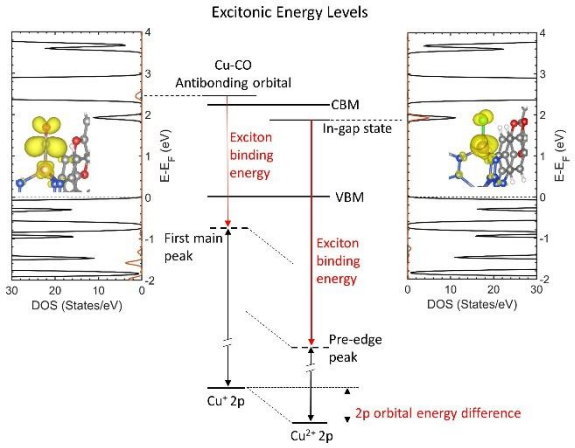

Figure 3. The DOS of Cu^{I}-MFU-4*l* (black curves) highlighting the Cu 3d projected-DOS (orange curves) for Cu^{+} with an adsorbed CO molecule (left) and for the Cu^{2+}-Cl defect (right). The charge density contour plots of the Cu-CO antibonding orbital and the in-gap state are shown in the insets. The schematic energy-level diagram indicates the calculated core-exciton binding energy of the pre-edge peak and the first main peak. The red arrows indicate the large exciton binding energy, which represents the Coulombic attraction between the Cu 2p core-hole and 3d electron.

ε_{2p} – According to Table 1, it is clear that the difference in core-level binding energy of 2p orbitals on Cu ions with different oxidation states varies based on the employed XC functionals. As expected, Cu^{2+} has nominally one less valence electron to screen core electron excitations, so the binding energy of the Cu^{2+} 2p orbitals is greater than that of the Cu^{+} 2p orbitals. In addition, the degree of orbital mixing or electron transfer between the occupied Cu 3d orbitals and the surrounding ligands or adsorbates also affects the local valence population and thereby the associated 2p core orbital binding energy. For this reason, the magnitude of the so-called chemical shift, or difference in 2p orbital binding energy between Cu^{+} and Cu^{2+} indicates the degree of localization and atomic Cu 3d character of the in-gap orbital generated upon Cu oxidation. The greater the fraction of Hartree-Fock (HF) exact exchange in our chosen functionals, the larger this difference in 2p binding energy between Cu^{+} and Cu^{2+}, reflecting the tendency for exact exchange (or reduced self-interaction) to produce more localized orbitals and more ionic bonds. By this argument we can easily understand why the binding energy difference of Cu 2p orbitals in the M06-2X functional is the largest, given that it utilizes the largest fraction (54%) of exact exchange on the length-scale of the 3d orbital (see the associated Mulliken charge analysis in Table 1).

ε_f – From Table 1, we can see that as HF exchange increases from 15% to 54%, the HOMO-LUMO gap increases from 4.3 to 7.1 eV, which is consistent with previous reports where HF exchange increases the band gap[44–46]. The in-gap-state-HOMO gap follows a similar but more exaggerated trend, increasing from 1.8 to 6.7 eV. This is expected for the much more localized Cu 3d in-gap orbital, which becomes more atomic-like with increased exact exchange due to the reduction of self-interaction errors in the other 9 occupied 3d orbitals which are more stabilized in energy and more spatially localized.

E_{binding} – The core-exciton binding energies of the pre-edge peak and the first main peak are calculated with various functionals, including M06-2X, ωB97M-V, PBE0, HSE, and customized functionals with 15, 20, and 54% global HF exchange. The exciton binding energy of the pre-edge peak and first peak also increase with the HF exchange proportion. The unoccupied (in-gap) Cu 3d orbital of Cu^{2+} becomes more and more localized or atomic-like, which increases the Coulombic interaction between the 2p core hole and the Cu 3d electron upon formation of the core-excited state, increasing the exciton binding energy. This effect is not as pronounced for the first main peak binding energy of Cu^{+}, since it has less Cu 3d character as it involves a transition to a mixed and more spatially delocalized orbital with Cu 3d and adsorbate LUMO character.

Long-range HF exact exchange is important for describing the binding energy of more delocalized excitations within LR-TDDFT [47], and a range-separated functional, such as ωB97M-V (with α = 100% at long range) may more accurately describe the delocalized excited state of the first main peak of Cu^{+} with more than double the binding energy of a global hybrid tuned to the same short-range exact exchange component (15%). By contrast, the M06-2X functional has a global 54% HF exchange (affecting both localized and delocalized excitations) and over-estimates the relative energy of the Cu^{2+} pre-edge peak due to almost doubling its binding energy. Clearly, excited states of different character are impacted differently by our choice of hybrid functional.

In our previous work, we used M06-2X LR-TDDFT to simulate the XAS of different molecules attached on the Cu^{+} site in the MOF. Due to the similar weak mixing between Cu 3d and the LUMOs of the attached molecules, the relative position of the first main peak for different molecules is consistent with experiment, which could be viewed as fortuitous cancellation of errors when comparing similar chemistries. However, in the present case, core-excitations of Cu^{+} and Cu^{2+} access quite different orbitals with differing sensitivity to α. Previous studies indicate that range-separated hybrid functionals often outperform global hybrid functionals[48–50], due to expected variations in Coulombic screening at different length scales. And, indeed, in the current case, focusing on core-excitations into orbitals with varying 3d character and spatial localization, ωB97M-V provides the best comparison with experiment among all the functionals tested in LR-TDDFT, including the best pre-edge peak to first peak energy difference and good XAS peak profile. However, this agreement is not precisely due to the relative accuracy of the XC functional used, but rather is more related to general shortcomings within the LR-TDDFT approach itself.

Multiple methodologies[51,52] have been proposed to correct LR-TDDFT calculations. The ΔSCF approach models specific excited states and their total energies self-consistently. In this study, we employed the maximum overlap method (MOM) to approximate 2p-core-excited state total energies for the first strong transitions of chemically distinct Cu atoms. We then substituted the ΔSCF total energy difference as the relative energy between the same (or most similar) transitions in our LR-TDDFT calculations. As shown in Figs. 1 and S2, with the ΔSCF correction, the simulated XAS calculated with ωB97M-V and M06-2X functionals are both consistent with the experiment.

We rationalize this inconsistency issue before performing the ΔSCF correction as follows: We excite Cu^{2+} from $2p^6 3d^9$ to $2p^5 3d^{10}$. The filling of an additional 3d orbital will lead to significant repulsive interactions with the other 9 3d electrons. Strong on-site repulsive Coulomb interactions between localized orbitals on the core-excited atom would raise the energy of the excited state. This should be captured within the ΔSCF approach. However, the orbital space used in LR-TDDFT only includes explicit interactions (i.e., matrix elements) between occupied core orbitals and unoccupied valence orbitals. So, while LR-TDDFT does describe the important attractive interactions between Cu 2p and 3d orbitals, which define strong core-exciton binding, it neglects the repulsive 3d-3d interactions (between the newly excited 3d electron and the original 9 occupied 3d electrons). This repulsive interaction should raise the excitation energy and reduce the binding energy. The missing onsite 3d-3d repulsion is quite small in the excited states of Cu^{+}, since the only available 3d character in the virtual orbitals is a small amount through mixing, and the occupied orbitals define a nominal $3d^{10}$ state. So Cu^{+} has a smaller error than Cu^{2+} due to missing onsite repulsion in LR-TDDFT. The size of this error should scale with α. Lower α means less localized orbitals and smaller onsite repulsion, thereby decreasing the Cu^{2+} binding energy and finally reducing the relative energy difference between Cu^{2+} and Cu^{+}, whereas higher α does the opposite. The M06-2X functional has high HF exchange in the short range and thus the Cu 3d orbital is over localized, which exaggerates the error.

Finally, if a given functional does in fact generate good relative LR-TDDFT energies for excited states of different character (such as Cu^{2+} and Cu^{+}), this could still be due to good fortune rather than increased accuracy, since the LR-TDDFT approach, as applied to core excitations, neglects repulsion between excited electrons and the remaining N-1 electrons, being written as a single electron-hole pair theory. We would need to find a way to include electron-electron repulsion terms to fix this issue in the future. Or, we would require that the functional should provide accurate estimates for electron addition and removal energies via its orbital energies (satisfying Janak's or Koopman's theorem) before applying it within a perturbative method such as LR-TDDFT.

One of the great advantages of LR-TDDFT for XAS simulations is that it can provide roots describing core-excitations across multiple atoms if the space of hole orbitals includes them. However, the lack of error cancellation between core-excitations of significantly different character indicates that the more careful approach is to perform separate LR-TDDFT calculations for each core-excited atom with a more accurate relative alignment provided by ΔSCF calculations.

Now we return to the origin of the energy ordering of the L_3-edge peaks in this case. Since Cu^{+} ($3d^{10}$) nominally has a fully occupied d shell, the virtual orbitals accessed that define the L_3-edge peak have very little Cu 3d orbital contribution and are spatially delocalized over multiple atoms, whereas Cu^{2+} ($3d^{9}$)

nominally has one fully unoccupied 3d orbital. According to Table 1, as the oxidation state of Cu increases from +1 to +2, the Cu 2p orbital binding energy increases by 2.85 eV when using the ωB97M-V functional, which would blue-shift the Cu^{2+} peak by the same amount, if the same valence orbital were accessed. However, the accessed orbital changes from an antibonding Cu 3d–CO LUMO at 9.06 eV above the HOMO for Cu^{+} to an in-gap, atomic-like Cu 3d orbital at 7.07 eV above the HOMO for Cu^{2+}, providing a net 1.99 eV spectral red shift, which does not quite cancel the 2.85 eV blue shift due to changes in core-orbital binding energy. Finally, the more localized Cu^{2+} 3d orbital accessed in the X-ray excitation exhibits a much stronger core-exciton binding energy (11.38 eV) than the antibonding and delocalized orbital accessed upon exciting the Cu^{+} 2p core-electron (5.50 eV). The resulting approximate energy difference would place the Cu^{2+} pre-edge peak 5.02 eV lower in energy than the Cu^{+} main peak. The actual LR-TDDFT result places the pre-edge peak 4.27 eV lower in energy and the ΔSCF corrects this to be much closer to the experimentally observed energy difference of 3.8 eV.

The specific values of these various contributions to the shift in peak energies vary significantly with the amount of exact exchange employed in the functional, but the overall trend is the same in all cases, resulting in a lower peak energy for the higher oxidation state of Cu. By contrast, for most transition metals, while different oxidation states adjust the number of unoccupied 3d orbitals, the core-excited states that define the first strong XAS peaks always refer to excitations into localized 3d orbitals, with a smaller difference in 3d orbital energies and quite similar exciton binding energies. Therefore, these XAS peak positions will be dominated by the 2p core-orbital energy differences, which are proportional to oxidation state and, so, higher oxidation states of more open-shell transition metals will have XAS onsets occurring at higher energies.

Finally, we return to our prediction of the relative population of Cu^{2+} defects in the MOF. The XAS spectra of different structures calculated with the ωB97M-V functional are shown in Fig. 1 with the assumption of equal populations of Cu^{+} (defining the first main peak) and Cu^{2+} (defining the pre-edge peak) based on our molecular cluster models. The compositional ratio Cu^{2+}/Cu^{+} could be calculated with the experimental and theoretical pre-edge XAS peak to first main peak ratio (see SI for details). From Table S2, we can see that the average Cu^{2+}/Cu^{+} ratio for different Cu^{2+} defects is close to 0.12. We view Cu-H as an outlier due to its lower chemical stability and likelihood. Its higher ratio estimate results, as stated above, from a relatively weaker pre-edge spectral intensity for Cu^{2+} due to a weak orbital mixing between Cu and the attached hydrogen atom.

Conclusions

To summarize, Cu^{2+} defects in the MOF Cu^{I}-MFU-4*l* have been studied with first-principles theory, and Cu^{2+} was identified as the origin of the pre-edge peak observed in previous experiments. The reason for a lower energy 2p core-excited state for the higher Cu^{2+} oxidation state, despite its larger 2p orbital binding energy, is due to a significantly larger exciton binding energy between the 2p core orbital (the hole) and an almost atomic-like Cu 3d orbital (the electron), accessible due to the $3d^9$ electronic configuration of the Cu^{2+} ion. By contrast, the much weaker Cu 3d character of the unoccupied orbitals associated with the lower Cu^{+} oxidation state (nominally $3d^{10}$), due to their mixing and delocalization across the surrounding system, leads to a smaller exciton binding energy. This particular energy ordering is unique to late transition metals oxidized in d^9 and d^{10} electron configurations (such as Cu, Ag, and Au) and is at odds with the more typical energy ordering of the majority of transition metals, where the first XAS peak energies increase with oxidation state.

It is found that there is a strong variation of the relative energy between the calculated LR-TDDFT pre-edge peak of Cu^{2+} and the first main peak of Cu^{+} when using different XC functionals, especially with respect to the fraction of exact exchange employed in hybrid functionals. The LR-TDDFT method should be used with caution when calculating X-ray excited states of atoms in different oxidation states. Notably, the ΔSCF method is found to be an effective solution to fix the misalignment of the predicted XAS peaks by including orbital relaxation and the strong on-site Coulomb repulsion of occupied 3d orbitals. Based on the calculated spectral intensity ratio between both oxidation states, the estimated concentration ratio of Cu^{2+} in Cu^{I}-MFU-4*l* was found to be ~0.12. These simulations demonstrate the sensitivity of XAS for differentiating late transition metal oxidation states and varying degrees of orbital mixing, and shows the potential of using XAS for future studies of mixed-valence functional materials.

Conflicts of interest

There are no conflicts to declare.

Acknowledgements

This work was carried out as part of the Gas Phase Chemical Physics program within the Chemical Sciences Division of Lawrence Berkeley National Laboratory (LBNL) and was supported by the U.S. Department of Energy, Office of Science, Office of Basic Energy Sciences and supported by a User Project at The Molecular Foundry. G.M.S., B.R.B., W.S.D., and J.R.L. acknowledge support from the U.S. Department of Energy, Office of Science, Basic Energy Sciences, Chemical Sciences, Geosciences, and Biosciences Division under Contracts DE-AC02-05CH11231 (FWP number CH19DRI01) and DE-SC0019992. Supercomputer time was provided by the National Energy Research Scientific Computing Center (NERSC), the Lawrencium computational cluster administered by the High Performance Computing Services Group at LBNL, and High-Performance Computing (HPC) Platform of ShanghaiTech University.

References

1 J. Yano and V. K. Yachandra, X-ray absorption spectroscopy, *Photosynth. Res.*, 2009, **102**, 241.

2 F. de Groot, High-Resolution X-ray Emission and X-ray Absorption Spectroscopy, *Chem. Rev.*, 2001, **101**, 1779–1808.

3 W. Grünert and K. Klementiev, X-ray absorption spectroscopy principles and practical use in materials analysis, *Phys. Sci. Rev.*, 2020, **5**, 20170181.

4 P. Zimmermann, S. Peredkov, P. M. Abdala, S. DeBeer, M. Tromp, C. Müller and J. A. van Bokhoven, Modern X-ray spectroscopy: XAS and XES in the laboratory, *Coord. Chem. Rev.*, 2020, **423**, 213466.

5 W.-S. Yoon, M. Balasubramanian, K. Y. Chung, X.-Q. Yang, J. McBreen, C. P. Grey and D. A. Fischer, Investigation of the Charge Compensation Mechanism on the Electrochemically Li-Ion Deintercalated Li1-xCo1/3Ni1/3Mn1/3O2 Electrode System by Combination of Soft and Hard X-ray Absorption Spectroscopy, *J. Am. Chem. Soc.*, 2005, **127**, 17479–17487.

6 M. Giorgetti, A Review on the Structural Studies of Batteries and Host Materials by X-Ray Absorption Spectroscopy, *ISRN Mater. Sci.*, 2013, **2013**, 938625.

7 W.-S. Yoon, O. Haas, S. Muhammad, H. Kim, W. Lee, D. Kim, D. A. Fischer, C. Jaye, X.-Q. Yang, M. Balasubramanian and K.-W. Nam, In situ soft XAS study on nickel-based layered cathode material at elevated temperatures: A novel approach to study thermal stability, *Sci. Rep.*, 2014, **4**, 6827.

8 P. Shearing, Y. Wu, S. J. Harris and N. Brandon, In Situ X-Ray Spectroscopy and Imaging of Battery Materials, *Interface Mag.*, 2011, **20**, 43–47.

9 S.-Y. Chang, A. Uehara, S. G. Booth, K. Ignatyev, J. F. W. Mosselmans, R. A. W. Dryfe and S. L. M. Schroeder, Structure and bonding in Au(i) chloride species: a critical examination of X-ray absorption spectroscopy (XAS) data, *RSC Adv.*, 2015, **5**, 6912–6918.

10 K. M. G. Siegbahn, W. C. Price and D. W. Turner, A Discussion on photoelectron spectroscopy - Electron spectroscopy for chemical analysis (e.s.c.a.), *Philos. Trans. R. Soc. London. Ser. A, Math. Phys. Sci.*, 1970, **268**, 33–57.

11 P. Jiang, D. Prendergast, F. Borondics, S. Porsgaard, L. Giovanetti, E. Pach, J. Newberg, H. Bluhm, F. Besenbacher and M. Salmeron, Experimental and theoretical investigation of the electronic structure of Cu2O and CuO thin films on Cu(110) using x-ray photoelectron and absorption spectroscopy, *J. Chem. Phys.*, 2013, **138**, 24704.

12 H. MASAI, M. KOSHIMIZU, H. KAWAMOTO, T. OHKUBO, A. KOREEDA, Y. FUJII, K. OHARA, H. OFUCHI and H. SETOYAMA, X-ray absorption near-edge structure of Ag cations in phosphate glasses for radiophotoluminescence applications, *J. Ceram. Soc. Japan*, 2019, **127**, 924–930.

13 R. K. Hocking, E. C. Wasinger, F. M. F. de Groot, K. O. Hodgson, B. Hedman and E. I. Solomon, Fe L-Edge XAS Studies of K4[Fe(CN)6] and K3[Fe(CN)6]: A Direct Probe of Back-Bonding, *J. Am. Chem. Soc.*, 2006, **128**, 10442–10451.

14 I. M. DiMucci, J. T. Lukens, S. Chatterjee, K. M. Carsch, C. J. Titus, S. J. Lee, D. Nordlund, T. A. Betley, S. N. MacMillan and K. M. Lancaster, The Myth of d8 Copper(III), *J. Am. Chem. Soc.*, 2019, **141**, 18508–18520.

15 W. S. Drisdell, R. Poloni, T. M. McDonald, J. R. Long, B. Smit, J. B. Neaton, D. Prendergast and J. B. Kortright, Probing Adsorption Interactions in Metal–Organic Frameworks using X-ray Spectroscopy, *J. Am. Chem. Soc.*, 2013, **135**, 18183–18190.

16 J. A. Mason, M. Veenstra and J. R. Long, Evaluating metal–organic frameworks for natural gas storage, *Chem. Sci.*, 2014, **5**, 32–51.

17 In *Introduction to Reticular Chemistry*, John Wiley & Sons, Ltd, 2019, pp. 295–311.

18 M. Dincă and J. R. Long, Hydrogen Storage in Microporous Metal–Organic Frameworks with Exposed Metal Sites, *Angew. Chemie Int. Ed.*, 2008, **47**, 6766–6779.

19 B. R. Barnett, H. A. Evans, G. M. Su, H. Z. H. Jiang, R. Chakraborty, D. Banyeretse, T. J. Hartman, M. B. Martinez, B. A. Trump, J. D. Tarver, M. N. Dods, L. M. Funke, J. Börgel, J. A. Reimer, W. S. Drisdell, K. E. Hurst, T. Gennett, S. A. FitzGerald, C. M. Brown, M. Head-Gordon and J. R. Long, Observation of an Intermediate to H2 Binding in a Metal–Organic Framework, *J. Am. Chem. Soc.*, 2021, **143**, 14884–14894.

20 J.-R. Li, R. J. Kuppler and H.-C. Zhou, Selective gas adsorption and separation in metal–organic frameworks, *Chem. Soc. Rev.*, 2009, **38**, 1477–1504.

21 B. R. Barnett, M. I. Gonzalez and J. R. Long, Recent Progress Towards Light Hydrocarbon Separations Using Metal–Organic Frameworks, *Trends Chem.*, 2019, **1**, 159–171.

22 Y. Wang and D. Zhao, Beyond Equilibrium: Metal–Organic Frameworks for Molecular Sieving and Kinetic Gas Separation, *Cryst. Growth Des.*, 2017, **17**, 2291–2308.

23 R. L. Siegelman, P. J. Milner, E. J. Kim, S. C. Weston and J. R. Long, Challenges and opportunities for adsorption-based CO2 capture from natural gas combined cycle emissions, *Energy Environ. Sci.*, 2019, **12**, 2161–2173.

24 D. Yang and B. C. Gates, Catalysis by Metal Organic Frameworks: Perspective and Suggestions for Future Research, *ACS Catal.*, 2019, **9**, 1779–1798.

25 A. Bavykina, N. Kolobov, I. S. Khan, J. A. Bau, A. Ramirez and J. Gascon, Metal–Organic Frameworks in Heterogeneous Catalysis: Recent Progress, New Trends, and Future Perspectives, *Chem. Rev.*, 2020, **120**, 8468–8535.

26 C. H. Hendon, A. J. Rieth, M. D. Korzyński and M. Dincă, Grand Challenges and Future Opportunities for Metal–Organic Frameworks, *ACS Cent. Sci.*, 2017, **3**, 554–563.

27 S. J. George, M. D. Lowery, E. I. Solomon and S. P. Cramer, Copper L-edge spectral studies: a direct experimental probe of the ground-state covalency in the blue copper site in plastocyanin, *J. Am. Chem. Soc.*, 1993, **115**, 2968–2969.

28 G. M. Su, H. Wang, B. R. Barnett, J. R. Long, D. Prendergast and W. S. Drisdell, Backbonding contributions to small molecule chemisorption in a metal–organic framework with open copper(i) centers, *Chem. Sci.*, 2021, **12**, 2156–2164.

29 G. Kresse and J. Furthmüller, Efficiency of ab-initio total energy calculations for metals and semiconductors using a plane-wave basis set, *Comput. Mater. Sci.*, 1996, **6**, 15–50.

30 G. Kresse and J. Furthmüller, Efficient iterative schemes for ab initio total-energy calculations using a plane-wave basis set, *Phys. Rev. B*, 1996, **54**, 11169–11186.

31 G. Kresse and D. Joubert, From ultrasoft pseudopotentials to the projector augmented-wave method, *Phys. Rev. B*, 1999, **59**, 1758–1775.

32 P. Blöchl, Projector augmented-wave method, *Phys. Rev. B*, 1994, **50**, 17953.

33 K. Lee, É. D. Murray, L. Kong, B. I. Lundqvist and D. C. Langreth, Higher-accuracy van der Waals density functional, *Phys. Rev. B*, 2010, **82**, 81101.

34 G. W. Mann, K. Lee, M. Cococcioni, B. Smit and J. B. Neaton, First-principles Hubbard U approach for small molecule binding in metal-organic frameworks, *J. Chem. Phys.*, 2016, **144**, 174104.

35 F. Weigend and R. Ahlrichs, Balanced basis sets of split valence{,} triple zeta valence and quadruple zeta valence quality for H to Rn: Design and assessment of accuracy, *Phys. Chem. Chem. Phys.*, 2005, **7**, 3297–3305.

36 N. A. Besley, Calculation of the electronic spectra of molecules in solution and on surfaces, *Chem. Phys. Lett.*, 2004, **390**, 124–129.

37 A. Dreuw and M. Head-Gordon, Single-Reference ab Initio Methods for the Calculation of Excited States of Large Molecules, *Chem. Rev.*, 2005, **105**, 4009–4037.

38 Y. Shao, Z. Gan, E. Epifanovsky, A. T. B. Gilbert, M. Wormit, J. Kussmann, A. W. Lange, A. Behn, J. Deng, X. Feng, D. Ghosh, M. Goldey, P. R. Horn, L. D. Jacobson, I. Kaliman, R. Z. Khaliullin, T. Kuś, A. Landau, J. Liu, E. I. Proynov, Y. M. Rhee, R. M. Richard, M. A. Rohrdanz, R. P. Steele, E. J. Sundstrom, H. L. W. III, P. M. Zimmerman, D. Zuev, B. Albrecht, E. Alguire, B. Austin, G. J. O. Beran, Y. A. Bernard, E. Berquist, K. Brandhorst, K. B. Bravaya, S. T. Brown, D. Casanova, C.-M. Chang, Y. Chen, S. H. Chien, K. D. Closser, D. L. Crittenden, M. Diedenhofen, R. A. D. Jr., H. Do, A. D. Dutoi, R. G. Edgar, S. Fatehi, L. Fusti-Molnar, A. Ghysels, A. Golubeva-Zadorozhnaya, J. Gomes, M. W. D. Hanson-Heine, P. H. P. Harbach, A. W. Hauser, E. G. Hohenstein, Z. C. Holden, T.-C. Jagau, H. Ji, B. Kaduk, K. Khistyaev, J. Kim, J. Kim, R. A. King, P. Klunzinger, D. Kosenkov, T. Kowalczyk, C. M. Krauter, K. U. Lao, A. D. Laurent, K. V Lawler, S. V Levchenko, C. Y. Lin, F. Liu, E. Livshits, R. C. Lochan, A. Luenser, P. Manohar, S. F. Manzer, S.-P. Mao, N. Mardirossian, A. V Marenich, S. A. Maurer, N. J. Mayhall, E. Neuscamman, C. M. Oana, R. Olivares-Amaya, D. P. O'Neill, J. A. Parkhill, T. M. Perrine, R. Peverati, A. Prociuk, D. R. Rehn, E. Rosta, N. J. Russ, S. M. Sharada, S. Sharma, D. W. Small, A. Sodt, T. Stein, D. Stück, Y.-C. Su, A. J. W. Thom, T. Tsuchimochi, V. Vanovschi, L. Vogt, O. Vydrov, T. Wang, M. A. Watson, J. Wenzel, A. White, C. F. Williams, J. Yang, S. Yeganeh, S. R. Yost, Z.-Q. You, I. Y. Zhang, X. Zhang, Y. Zhao, B. R. Brooks, G. K. L. Chan, D. M. Chipman, C. J. Cramer, W. A. G. III, M. S. Gordon, W. J. Hehre, A. Klamt, H. F. S. III, M. W. Schmidt, C. D. Sherrill, D. G. Truhlar, A. Warshel, X. Xu, A. Aspuru-Guzik, R. Baer, A. T. Bell, N. A. Besley, J.-D. Chai, A. Dreuw, B. D. Dunietz, T. R. Furlani, S. R. Gwaltney, C.-P. Hsu, Y. Jung, J. Kong, D. S. Lambrecht, W. Liang, C. Ochsenfeld, V. A. Rassolov, L. V Slipchenko, J. E. Subotnik, T. Van Voorhis, J. M. Herbert, A. I. Krylov, P. M. W. Gill and M. Head-Gordon, Advances in molecular quantum chemistry contained in the Q-Chem 4 program package, *Mol. Phys.*, 2015, **113**, 184–215.

39 D. Denysenko, M. Grzywa, J. Jelic, K. Reuter and D. Volkmer, Scorpionate-Type Coordination in MFU-4l Metal–Organic Frameworks: Small-Molecule Binding and Activation upon the Thermally Activated Formation of Open Metal Sites, *Angew. Chemie Int. Ed.*, 2014, **53**, 5832–5836.

40 S. A. FitzGerald, D. Mukasa, K. H. Rigdon, N. Zhang and B. R. Barnett, Hydrogen Isotope Separation within the Metal–Organic Framework Cu(I)-MFU-4l, *J. Phys. Chem. C*, 2019, **123**, 30427–30433.

41 M. C. Neary and G. Parkin, Dehydrogenation{,} disproportionation and transfer hydrogenation reactions of formic acid catalyzed by molybdenum hydride compounds, *Chem. Sci.*, 2015, **6**, 1859–1865.

42 J. Lücken, T. Auth, S. I. Mozzi and F. Meyer, Hexanuclear Copper(I) Hydride from the Reduction-Induced Decarboxylation of a Dicopper(II) Formate, *Inorg. Chem.*, 2020, **59**, 14347–14354.

43 C. K. Brozek and M. Dincă, Cation exchange at the secondary building units of metal–organic frameworks, *Chem. Soc. Rev.*, 2014, **43**, 5456–5467.

44 P. J. Hasnip, K. Refson, M. I. J. Probert, J. R. Yates, S. J. Clark and C. J. Pickard, Density functional theory in the solid state, *Philos. Trans. R. Soc. A Math. Phys. Eng. Sci.*, 2014, **372**, 20130270.

45 H. Xiao, J. Tahir-Kheli and W. A. Goddard, Accurate Band Gaps for Semiconductors from Density Functional Theory, *J. Phys. Chem. Lett.*, 2011, **2**, 212–217.

46 J. P. Perdew, W. Yang, K. Burke, Z. Yang, E. K. U. Gross, M. Scheffler, G. E. Scuseria, T. M. Henderson, I. Y. Zhang, A. Ruzsinszky, H. Peng, J. Sun, E. Trushin and A. Görling, Understanding band gaps of solids in generalized Kohn{\textendash}Sham theory, *Proc. Natl. Acad. Sci.*, 2017, **114**, 2801.

47 J.-C. Lee, J.-D. Chai and S.-T. Lin, Assessment of density functional methods for exciton binding energies and related optoelectronic properties, *RSC Adv.*, 2015, **5**, 101370–101376.

48 P. Rivero, I. de P. R. Moreira, F. Illas and G. E. Scuseria, Reliability of range-separated hybrid functionals for describing magnetic coupling in molecular systems, *J. Chem. Phys.*, 2008, **129**, 184110.

49 P. Rivero, I. de P. R. Moreira, G. E. Scuseria and F. Illas, Description of magnetic interactions in strongly correlated

solids via range-separated hybrid functionals, *Phys. Rev. B*, 2009, **79**, 245129.

50 U. Salzner and A. Aydin, Improved Prediction of Properties of π-Conjugated Oligomers with Range-Separated Hybrid Density Functionals, *J. Chem. Theory Comput.*, 2011, **7**, 2568–2583.

51 S. G. Minasian, J. M. Keith, E. R. Batista, K. S. Boland, D. L. Clark, S. A. Kozimor, R. L. Martin, D. K. Shuh and T. Tyliszczak, New evidence for 5f covalency in actinocenes determined from carbon K-edge XAS and electronic structure theory, *Chem. Sci.*, 2014, **5**, 351–359.

52 P. Norman and A. Dreuw, Simulating X-ray Spectroscopies and Calculating Core-Excited States of Molecules, *Chem. Rev.*, 2018, **118**, 7208–7248.